Underhood thermal management: temperature and heat flux measurements and physical analysis

Mahmoud Khaled, Fabien Harambat, Hassan Peerhossaini

To cite this version:

Mahmoud Khaled, Fabien Harambat, Hassan Peerhossaini. Underhood thermal management: temperature and heat flux measurements and physical analysis. Applied Thermal Engineering, 2009, 30 (6-7), pp.590. ⟨10.1016/j.applthermaleng.2009.11.003⟩. ⟨hal-00544813⟩

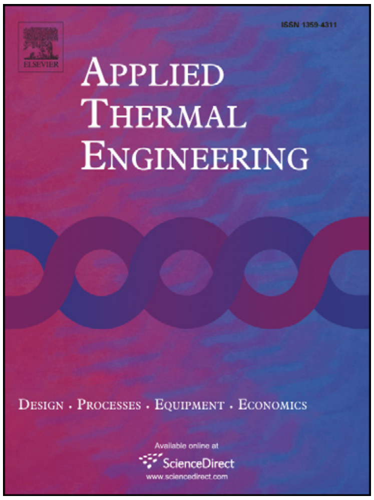

Underhood thermal management: temperature and heat flux measurements and physical analysis

Mahmoud Khaled, Fabien Harambat, Hassan Peerhossaini

PII: S1359-4311(09)00331-7
DOI: 10.1016/j.applthermaleng.2009.11.003
Reference: ATE 2921

To appear in: *Applied Thermal Engineering*

Received Date: 27 April 2009
Accepted Date: 5 November 2009

Please cite this article as: M. Khaled, F. Harambat, H. Peerhossaini, Underhood thermal management: temperature and heat flux measurements and physical analysis, *Applied Thermal Engineering* (2009), doi: 10.1016/j.applthermaleng.2009.11.003

Underhood thermal management: temperature and heat flux measurements and physical analysis

Mahmoud Khaled[1,2], Fabien Harambat[2], Hassan Peerhossaini[1]

1 Thermofluids, complex flows and energy research group - Laboratoire de Thermocinétique, CNRS-UMR 6607, Ecole polytechnique de l'université de Nantes, rue C.Pauc, BP 50609, 44 306 Nantes cedex 3 - France

2 PSA Peugeot Citroën – Velizy A Center, 2 route de Gisy, 78 943 Vélizy Villacoublay – France

Corresponding author: Tel.: +33.2.40.68.31.24; Fax: +33.2.40.68.31.41.
E-mail addresses: hassan.peerhossaini@univ-nantes.fr

Abstract

Aerodynamic cooling drag, caused by car underhood cooling, can be reduced by better underhood aerothermal management. This study addresses the aerothermal phenomena encountered in the vehicle underhood compartment by physical analysis of the heat transfer modes in complex internal flows. We report here underhood heat flux and temperature measurements on a vehicle in wind tunnel S4 of Saint-Cyr-France using a new experimental method. The underhood is instrumented by 40 surface and air thermocouples and 20 fluxmeters. Measurements are carried out for three thermal functioning points: the engine in operation and the front wheels positioned on the test facility with power-absorption-controlled rollers. The ultimate aim is to reengineer the underhood architecture so as to reduce the cooling air flow rate in the underhood component and hence the aerothermal cooling drag.

Keywords: Aerodynamic cooling drag, underhood aerothermal management, separated heat flux method, convective heat transfer, radiative heat transfer.

Nomenclature

G_R	Gear ratio
h_c	Convection coefficient, $W.m^{-1}.K^{-1}$
n	Engine regime, rpm
P	Wheel power, kW
T	Temperature, $°C$
T_a	Air temperature, $°C$
$T_{\max}$	Maximal temperature, $°C$
T_p	Surface temperature, $°C$
T_0	Initial temperature, $°C$
$TFP-1$	Thermal functioning point 1
$TFP-2$	Thermal functioning point 2
$TFP-3$	Thermal functioning point 3
V_{air}	Air velocity near tested component, $Km.h^{-1}$
V_W	Wheel speed, $Km.h^{-1}$
V_{wind}	Wind speed, $Km.h^{-1}$
ΔT	Temperature difference between surface and surrounding air, $°C$
φ	Heat flux density, $W.m^{-2}$
$\varphi_{\max}$	Maximal heat flux density, $W.m^{-2}$
φ_0	Initial heat flux density, $W.m^{-2}$
φ_∞	Heat flux density at end of constant-speed driving phase, $W.m^{-2}$
φ_c	Convective heat flux density, $W.m^{-2}$
$\varphi_{c,\max}$	Maximal convective heat flux density, $W.m^{-2}$
$\varphi_{c,0}$	Initial convective heat flux density, $W.m^{-2}$
$\varphi_{c,\infty}$	Convective heat flux density at end of constant-speed driving phase, $W.m^{-2}$
φ_r	Radiative heat flux density, $W.m^{-2}$
$\varphi_{r,\max}$	Maximal radiative heat flux density, $W.m^{-2}$
$\varphi_{r,0}$	Initial radiative heat flux density, $W.m^{-2}$
$\varphi_{r,\infty}$	Radiative heat flux density at end of constant-speed driving phase, $W.m^{-2}$
τ	Time constant, s

1- Introduction

The energy necessary to drive an automobile is essentially produced by fuel combustion in the engine. The gas temperatures at the end of combustion in the front flame are around 1500 – 2000 °C. To prevent damage to the cylinder walls by high-temperature gases upon combustion, the engine must be cooled drastically by water circulation in the engine jacket (cooling system). At the same time, mechanical components in the underhood environment must not undergo thermal loads so great that they risk wearing out prematurely. It is thus essential to cool the underhood region by a flow of external air that enters the underhood through its air inlet openings at a specified vehicle speed and is sufficient to cool the components in all areas of the underhood compartment. Thus both underhood cooling and the water cooling system impose losses in the primary-to-mechanical energy conversion.

Consider a 435-hp Porsche 911 GT3 engine and a 215-hp Citroen C6 3.0i V6. For each car the thermal energy lost by heat transfer in the engine compartment is of the same order of the engine power (435-hp and 215-hp respectively). Recovery of 17% of the sum of energy lost in the above two cars would suffice to run a 105-hp Renault Megane II 1.5 DCI passenger car.

In addition, underhood air penetration increases the vehicle's overall aerodynamic drag: the contribution to the overall aerodynamic drag called aerodynamic cooling drag that is tightly correlated with the air flow rate entering the underhood compartment. The aerodynamic cooling drag (car energy consumption) can be reduced by better underhood aerothermal management, i.e. more cooling with less air flow. Understanding the convective and radiative heat transfer is a first step in underhood aerothermal management that lets us avoid overestimating the air flow rate necessary to cool the underhood region, thus reducing the aerodynamic cooling air drag caused by the supplementary entering air.

In automotive development projects, car design is under strict specifications. It must satisfy geometric restrictions induced by styling constraints and must be oriented to high-performance engines and well controlled climate systems. To manage this dual goal, a large number of components must be implemented in small underhoods containing thermal systems (cooling, air conditioning, and air charging) that are already too large and complex to meet additional thermal performance requirements. In addition, noise reduction criteria have augmented the use of insulation around the underhood compartment. These underhood aerothermal specifications give rise to airflows in the confined underhood space that are complex aerothermal phenomena involving internal flow topology, convective heat transfer in interaction with internal flow topology, and radiative heat transfer in conjunction with convective transfer.

Internal flows are flows of fluid in a wall-limited space of a duct or a closed cavity with which the fluid exchanges heat by convection. There is a strong relation between the nature of the fluid and the interior geometry of the flow passage. Fluid flow and heat transfer phenomena in simple internal flows are well understood. However, they become more difficult when one faces complex geometries, for example that encountered in the actual vehicle underhoods described above. In addition the geometries in the underhood compartment are at a large scale compared to those in classical internal flows.

Flows in the vehicle underhood are thus large-scale complex internal flows in which the fluid (air) faces complex geometries and different hot surfaces (components) that themselves exchange heat with the environment by radiation, and complex heat-transfer phenomena (convection and radiation) thus arise in the confined underhood geometry. In addition, convective and radiative heat transfer normally occurs simultaneously in the underhood and measured heat flux densities are global densities (the sum of convective and radiative heat flux densities). To analyze the underhood aerothermal behavior properly, it is indispensable to characterize each phenomenon (convection or radiation) separately. We present here a new method by which measurement of convective heat flux density is separated from that of radiative heat flux density.

Experimental studies [1, 2, 3, and 4] on the understanding of these phenomena are rare and the literature refers instead to numerical simulations [5, 6, and 7]; however, these simulations are not accurate enough to estimate temperatures and heat flux in the underhood. In addition, numerical simulations must be validated experimentally and necessitate experimental boundary conditions [8, 9, 10, 11, and 12].

Here we report temperature and heat flux measurements carried out on a vehicle in a wind tunnel in order to better understand thermal conditions in the underhood. Section 2 describes the underhood instrumentation and test configurations, section 3 analyzes the temperature and heat flux (overall, convective, and radiative) behaviors obtained from the underhood measurements, and section 4 gives our conclusions.

2- Measurements and experimental procedures

The principle of the measurement of convective and radiative heat flux densities is based on the separation of the overall heat flux density into two parts: radiataive and convective fluxes [13 – 15]. The idea is to fix on a surface of known emissivity two fluxmeters of different emissivities (black and bright aluminum for example). In this case, the two fluxmeters will measure different overall heat flux densities corresponding of the same convective heat fluxs but different radiative heat fluxes. Then, one can calculate separately, knowing the surface emissivities, the convective and the radiative heat fluxes.

In the following, convective heat flux is considered “positive” if heat is transferred from air to solid surface, and is called negative in the opposite case.

The experimental setup and methods used in this work are detailed in [16]; here we present a brief description. Aerothermal experiments were carried out on a vehicle in the wind tunnel of the Saint-Cyr l’Ecole-France for the three thermal functioning points in table 1. The car engine is functioning and the front wheels are positioned on test facility rollers so as to adjust and control their power and rotational speed. For each experimental run (fixed thermal functioning point), data recording (heat flux and temperatures) covers three successive phases: the constant-speed driving, slowdown, and thermal soak phases. The constant-speed driving phase simulates the actual driving of a vehicle; it can be TFP-1, TFP-2, or TFP-3. The slowdown phase is simulated in the wind tunnel by going to the neutral point after the constant-speed driving phase and stopping the wind-tunnel airflow. Thermal soak corresponds to the stopping the vehicle after a high thermal charge.

The underhood of the car used in these experiments is instrumented by type T surface and air thermocouples and 20 normal-gradient fluxmeters. The regions tested are the cold box (side, upstream, and top), air filter, cylinder head cover, inlet and outlet ducts of the charge air cooler (CAC), and the engine side. The normal-gradient fluxmeters are fixed in pairs at 10 components in the underhood compartment. Figure 1 shows a schematic top view of the different components instrumented in the underhood compartment.

3- Results and discussions

3.1- The separation method

We consider (Figure 2) the evolution of the heat flux densities measured by the two fluxmeters (black and aluminum) at the side wall of the cold box for TFP-3, and observe that the two fluxmeters do not measure the same overall heat flux density in the constant-speed and thermal soak phases. Heat flux densities are non-dimensionalized by the heat flux density measured by the black fluxmeter at the beginning of the experimental run. For example, at the end of the constant-speed driving phase, we have an overall heat flux density of $0.13\varphi_0$ measured by the black fluxmeter and about $-0.08\varphi_0$ measured by the aluminum fluxmeter. At the end of thermal soak, we find overall heat flux densities of $0.23\varphi_0$ with the black fluxmeter and $-0.07\varphi_0$ with the aluminum fluxmeter. Using these differences in the overall heat flux density measurements by the two fluxmeters, we can separate the convective heat flux density from the radiative density.

Figure 3 shows the evolution of the overall, convective and radiative heat flux densities obtained from the measurements of the two fluxmeters at the cold box side in TFP-3. We see that the overall heat flux density of $0.13\varphi_0$ measured at the end of the constant-speed driving phase is the resultant of a convective heat flux density of $0.25\varphi_0$ and a radiative heat flux density of $-0.12\varphi_0$, and that at the end of the thermal soak phase, the overall density of $0.23\varphi_0$ is the resultant of a convective density of $0.25\varphi_0$ and a radiative density of $-0.02\varphi_0$. Thus, the overall heat flux density in the constant-speed driving phase is the convective heat flux density with a negative offset corresponding to the radiative density. In thermal soak, the overall density is almost equal to the convective heat flux density.

Let us now analyze the convective heat flux density evolution at the cold box side wall (Figure 4b) during the three successive phases in relation to the evolution of the surface and air temperatures (Figure 4a). The evolutions can be divided into three intervals with respect to convection type:

1- the first interval ($[0;t_1]$) corresponds to the constant-speed driving and slowdown phases. In this interval, convection is mixed convection with predominant forced convection, especially in constant-speed driving. In the constant-speed driving phase, we observe increases in the surface and air temperature with time. In addition, at the beginning the surface temperature increases more rapidly than the air temperature, resulting in decreased positive convective heat flux density during constant-speed driving. In the slowdown phase $[t_1;t_1^{'}]$, the air temperature increases more rapidly than the surface temperature, resulting in increased positive convective density.

2- the second interval ($[t_1^{'};t_3]$) corresponds to the first part of the thermal soak phase in which the fan goes to its low rotational speed. In this interval, convection is forced convection; thermal inertia is preserved and no heat is produced (no combustion), so that the air temperature decreases very rapidly relative to the surface temperature (which also decreases) and we observe a decreased positive convective density. At t_2, the surface and air temperatures are equal and the convective density tends to zero. After t_2, the air temperature continues to decrease rapidly and the surface temperature becomes higher, increasing the absolute value of the negative convective heat flux density.

3- the third interval ($t > t_3$) corresponds to the second part of the thermal soak in which the fan stops completely. In this interval, convection is only natural convection. Therefore, with the components at thermal inertia, the air temperature starts to increase even more rapidly than the surface temperature (no forced air flow to the underhood), and we thus observe a decrease in absolute value of the negative convective heat flux density. At t_4, the air and surface temperatures become the same and the convective density become zero. After t_4, the air temperature and surface temperature increase briefly before becoming almost constant, as does the convective density at the end of the thermal soak phase.

None of these thermal behaviors at the cold-box side can be explained from the overall heat flux density alone. Therefore, we must separate the convective and radiative heat flux densities in order to explain thermal behaviors and temperature-flux coupling.

Another feature of our heat flux separation method appears in the comparison between the three thermal functioning points. Consider the evolution of the overall heat flux density at the cold box side for the three thermal functioning points tested as shown on Figure 5-a. At the end of the constant-speed driving phase, the overall heat flux densities for the three thermal functioning points are very close. For example, we measure an overall heat flux density of $0.04\varphi_0$ at TFP-1, $0.10\varphi_0$ at TFP-2, and $0.11\varphi_0$ at TFP-3. One can consider that the thermal situation on the cold-box side does not differ among the different thermal functioning points; this is not the case, however, when we focus on the separate heat flux densities (convective and radiative) measured for the three different thermal functioning points at the same component (Figure 5b and 5c).

We observe that the close overall heat flux densities measured at the three thermal functioning points are the resultant of different convective and radiative heat flux densities. For example, at the end of the constant-speed driving phase, we measure convective heat flux densities of $0.49\varphi_0$ at TFP-1, a mean value of $0.43\varphi_0$ in TFP-2 and $0.21\varphi_0$ at TFP-3 and radiative heat flux densities of $-0.45\varphi_0$ at TFP-1, a mean value of $-0.33\varphi_0$ in TFP-2 and $-0.10\varphi_0$ at TFP-3. Hence the thermal situation on the cold-box side is not the same among the three thermal functioning points. This is the compensation between the convective and radiative heat flux densities (which compose the overall density) that imposes approximately the same overall heat flux density among the three thermal functioning points, especially TFP-2 and TFP-3

3.2- Underhood thermal behaviors

In the constant-speed driving phase and for the three test thermal functioning points, we have seen components that absorb heat by convection. These absorbed convective heat flux densities are the result of the passage of hot air that has extracted heat from components at higher temperatures, i.e. the air filter and the charge air cooler CAC outlet duct. Figure 6 shows the convective heat flux density evolution at the air filter and the charge air cooler outlet duct at TFP-1.

From Figure 6b, we observe that air zones near the air filter and the charge air cooler outlet duct are hotter than the surfaces; this causes convective heat densities to be absorbed at the surfaces of the two components, as shown in Figure 6a. For example, while at the end of the constant-speed driving phase we have temperatures of T_0 and $0.57T_0$ respectively in the air zones near the air filter and the CAC outlet duct, we measure surface temperatures of $0.76T_0$ and $0.52T_0$. Temperatures are non-dimensionalized with respect to the quasi-stabilization temperature of the air zone near the air filter (which is the highest temperature among the four temperatures on the graph). Therefore, exterior air entering the underhood to cool the engine compartment by convection does not necessarily cool all the components in the underhood region, because cold surfaces are positioned downstream of hot surfaces (for example, the air filter is downstream of the engine).

In both the constant-speed driving and the thermal soak phases and for the majority of the components tested, it is the convective heat flux density that imposes its trend on the overall heat flux density.

3.3- Temperature and heat flux trends

In the constant-speed driving phase, for the different thermal functioning points, typical exponential tendencies are observed for the temperature evolutions, and exponential tendencies have also been observed for the overall, convective, and radiative heat flux density time evolutions. The temperature evolution in the constant-speed driving phase follows the general exponential form:

$$T(t) = T_0 + (T_{\max} - T_0).\left[1 - \exp\left(-\frac{t}{\tau}\right)\right] \qquad (11)$$

where $T_{\max}$ is the maximum temperature attained at the surface of the component considered and τ is a time constant. $T_{\max}$ depends essentially on the component's component and the thermal functioning point and τ depends on the component's inertia.

The typical exponential forms of the overall, convective and radiative heat flux densities at the different components in the constant-speed driving phase follow the trends below:

$$\varphi = \varphi_0 + (\varphi_{\max} - \varphi_0).\left[1 - \exp\left(-\frac{t}{\tau}\right)\right] \quad (12)$$

$$\varphi = \varphi_\infty + (\varphi_0 - \varphi_\infty).\exp\left(-\frac{t}{\tau}\right) \quad (13)$$

$$\varphi_c = \varphi_{c,0} + (\varphi_{c,\max} - \varphi_{c,0}).\left[1 - \exp\left(-\frac{t}{\tau}\right)\right] \quad (14)$$

$$\varphi_c = \varphi_{c,\infty} + (\varphi_{c,0} - \varphi_{c,\infty}).\exp\left(-\frac{t}{\tau}\right) \quad (15)$$

$$\varphi_r = \varphi_{r,0} + (\varphi_{r,\max} - \varphi_{r,0}).\left[1 - \exp\left(-\frac{t}{\tau}\right)\right] \quad (16)$$

$$\varphi_r = \varphi_{r,\infty} + (\varphi_{r,0} - \varphi_{r,\infty}).\exp\left(-\frac{t}{\tau}\right) \quad (17)$$

where φ_0, $\varphi_{c,0}$ and $\varphi_{r,0}$ are respectively the global, convective and radiative heat flux densities at each component at the start of constant-speed driving, $\varphi_{\max}$, $\varphi_{c,\max}$ and $\varphi_{r,\max}$ are respectively the maximal overall, convective and radiative heat flux density (quasi-stabilized heat flux densities) and φ_∞, $\varphi_{c,\infty}$ and $\varphi_{r,\infty}$ are respectively the overall, convective and radiative heat flux densities at the end of constant-speed driving. φ_0, $\varphi_{c,0}$, $\varphi_{r,0}$, $\varphi_{\max}$, $\varphi_{c,\max}$, $\varphi_{r,\max}$, φ_∞, $\varphi_{c,\infty}$ and $\varphi_{r,\infty}$ can be either positive or negative, depending on whether the component absorbs heat from or yields heat to its environment, and depend essentially on the component of the element and the thermal functioning point.

Figure 7 compares curves of experimental data and theoretical exponential curves for temperature evolution at the cold-box side wall (Figure 7a) and for convective heat flux density evolution at the charge air cooler inlet duct for TFP-1 in the constant-speed driving phase (Figure 7b). We see here that temperature and convective heat flux density curves fit well with the theoretical exponential curves. For example, at the cold-box side, the mean gap between experimental and theoretical temperature evolution is 0.2°C (0.4%); at the charge air cooler duct, the mean gap between experimental and theoretical convective heat flux density evolution is 41 W/m² (4.3%). Comparisons of these orders of magnitude between theoretical and experimental evolutions are also found for overall and radiative heat flux densities, for all components tested and for all thermal functioning points, confirming the typical exponential tendencies of temperature and heat flux densities in the constant-speed driving phase.

In the thermal soak phase, we observed no typical tendencies in the different test components either for temperature or for heat flux density (overall, convective, or radiative). However, we have observed the presence of peaks and variations in the curves for the heat flux densities and temperatures that are related to changes in the type of convection during the thermal soak phase. In fact, at the beginning of the thermal soak the fan passes to its low rotational speed for few minutes before it stops completely. At the end of thermal soak, all temperatures measured in the underhood tend to the ambient temperature and all the overall heat flux densities tend to zero, both usually because of compensations between convective heat flux density and radiative heat flux density. All these tendencies appear in Figure 8, which shows sample temperature and heat flux density evolutions at the CAC outlet duct in thermal soak for TFP-1.

We see clearly in Figure 8b the changes in the trend of the convective heat flux density related to the fan operation mode. These changes impose changes in the overall heat flux densities, altering the temperature evolutions of Figure 8a. We observe an increase in the convective heat flux density in the first part of the phase due to hot air oriented by the low-speed fan; after the fan stops, convective heat transfer at the CAC outlet duct occurs only by natural convection from the hot surrounding air, which decreases in temperature more rapidly than the CAC outlet duct surface, decreasing the convective heat flux density. We can see that these behaviors of the convective heat flux density at the CAC outlet duct are reproduced in the overall heat flux density evolution: Figure 8b shows that the overall heat flux density also increases in the first part of thermal soak and decreases in the second. In addition, we observe that the tendency to zero at the end of thermal soak of the overall heat flux is induced by compensations between the convective and the radiative heat flux density tendencies shown in Figures 8b.

3.4- Thermal functioning points

Temperature-heat flux coupling

Temperatures and heat flux densities in the underhood vary with thermal functioning points since the engine power and air velocity in the underhood vary with different functioning points. Figure 9 shows dimensionless temperatures (calculated with respect to that in TFP-1) and overall heat flux densities at all the test components for the three different thermal functioning points.

From Figure 9a, we see that TFP-2 is the most thermally charged functioning point and TFP-1 is the least charged. These temperature tendencies can be explained by the overall heat flux tendencies among the different thermal functioning points in Figure 9b at some but not all of the test components. For example, at the cylinder head cover, the overall heat flux density in TFP-2 is positive, while in TFP-1 and TFP-3 they are negative; thus the cylinder head cover in TFP-2 absorbs heat while in TFP-1 and TFP-3 it releases heat. In addition, in TFP-1, the overall heat flux density is higher in absolute value than in TFP-3, and hence in TFP-1 the cylinder head cover releases more heat than in TFP-3. This is why we measure a higher temperature at the cylinder head cover in TFP-2, than in TFP-1 and finally in TFP-3.

However, on the cold-box above the coupling between the overall heat flux densities and temperatures is difficult to deduce. In TFP-2, we measure positive overall heat flux density (Figure 9b), which explains the highest temperature (Figure 9a) with respect to the negative densities measured in TFP-1 and TFP-3, However, between TFP-1 and TFP-3 the analysis is not clear. In fact, in TFP-3 the negative measured overall heat flux density is higher in absolute value than in TFP-1, but the temperature in TFP-1 is smaller. These behaviors are also observed at other components such as the CAC inlet and outlet ducts and the right engine elastomer. The difficulties in analyzing the overall heat flux density – temperature arise because:

- convection in the underhood region in the constant-speed driving phase is mixed convection and the different overall heat flux densities are not exchanged at the same temperatures
- the measured overall heat flux densities are measured at the component's surface, and are not the only heat flux densities affecting the surface temperature of the component

Therefore, we must appeal to heat flux separation (convective and radiative) of the overall heat flux densities in order to establish a typical coupling between heat flux density and temperature between the different thermal functioning points. By measuring the convective heat flux densities separately at the surface of the different components and calculating the convective heat transfer coefficient with respect to a fluid reference temperature of zero:

$$h_c = \frac{\varphi_c}{T_p} \quad (18)$$

we obtain the histogram in Figure 10 of the dimensionless convective heat transfer coefficients (calculated with respect to TFP-1 coefficients) at the different components for the three thermal functioning points. In fact, since in the underhood compartment the air temperature varies from one point to another, the choice of T_a for obtaining h from the equation $\varphi = h.(T_p - T_a)$ is not unique. To obviate this difficulty we opted to choose $T_a = 0$ to replace T_a in this equation. This new definition of the reference temperature makes h dependent of T_p, V_{air} and ΔT:

$$h_c = f(V_{air}; T_p; \Delta T) \quad (18)$$

For most of the tested components, we observe that convective heat transfer coefficients are highest in TFP-3, than in TFP-1 and finally in TFP-2.

Let us now compare TFP-2 and TFP-3. In TFP-3, air velocities near components are the greatest due to higher velocity speed. In addition, for negative convective heat flux densities, temperature differences are also the greatest in absolute value (since the air temperature is lower). On the other hand, surface temperatures are also higher in TFP-3 (more engine power) than in TFP-2. Then, for all test components in which heat is transferred from component to surrounding air, the two parameters V_{air} and ΔT increase and T_p decreases from TFP-2 to TFP-3. The increases in air velocity and temperature difference dominate the surface temperature decrease, resulting in increased convective heat transfer coefficients from TFP-2 to TFP-3. This explains why convective heat transfer coefficients are higher in TFP-3 than in TFP-2. For components where convective flux are absorbed (i.e. where surface temperature T_p is smaller than air temperature T_a), the two parameters ΔT and T_p decrease and

V_{air} increases. The air velocity increase is so significant between TFP-2 and TFP-3 that it dominates the decrease in surface temperature and temperature difference, resulting in increased convective heat transfer coefficients from TFP-2 to TFP-3.

For the comparison between TFP-3 and TFP-1, a similar analysis to that for the components in which convective heat flux is released explains why the convection coefficient is higher in TFP-3 than in TFP-1. For components of absorbed convective heat flux, the evolution of the convection coefficient between the two thermal points depends on components. For the absorbed convective flux, V_{air} and T_p increase and ΔT decreases: at the air filter, for example, the increases in air velocity and surface temperature dominate the temperature difference decrease from TFP-1 to TFP-3, resulting in increased convection coefficients in TFP-3 over TFP-1. Unlike the air filter on the cold-box side, the temperature difference is so much smaller in TFP-3 than in TFP-1 that its decrease dominates the air velocity and surface temperature increases, resulting in a decreased convection coefficient from TFP-1 to TFP-3.

Between TFP-1 and TFP-2, air velocities and temperature differences increase and surface temperatures decrease from TFP-2 to TFP-1 for released convective heat flux. For most of the test components, the air velocity and temperature difference increases dominate the surface temperature decrease from TFP-2 to TFP-1, resulting in increased convection coefficients in TFP-1 over TFP-2. For the absorbed convective flux, the convection coefficient evolution between the above two thermal points depends on component. For example, at the air filter, the increases in surface temperature and temperature difference from TFP-1 to TFP-2 dominate the air velocity decrease, resulting in increased convection coefficient in TFP-2 over TFP-1.

To establish the temperature-heat flux coupling, we consider Figure 11 which compares the three thermal functioning points for the mean convective heat transfer coefficient (between the tested components), engine power released in the underhood compartment, and mean temperature of the test components. Consider TFP-3 and TFP-2: the engine power in TFP-3 is higher than in TFP-2, but convective heat transfer coefficients are so much higher that they dominate the engine power increase, resulting in increased temperature in TFP-2 over TFP-3. Between TFP-1 and TFP-3, the convective heat transfer coefficients are higher in TFP-3 than in TFP-1 and the heat released from the engine is also higher in TFP-3, however the engine power released in the underhood compartment is so much higher in TFP-3 than TFP-1 that it dominates the increase in the convection coefficients in TFP-3, resulting in increased temperature in TFP-3 over TFP-1. Finally, between TFP-1 and TFP-2, the convective heat transfer coefficients in TFP-1 are higher than in TFP-2, but in TFP-2 the heat released by engine in the underhood compartment is so much higher than in TFP-1 that it dominates the increase in convection coefficients in TFP-1, resulting in increased temperature in TFP-2 over TFP-1.

Oscillatory behaviors

In TFP-2 in the constant-speed driving phase, we observed oscillatory behaviors in the evolution of the surface and air temperatures and the overall, convective and radiative heat flux densities. In effect, TFP-2 is not in fact a real thermal configuration with which a car can be confronted, but instead describes situations in which entering air is subjected to some circumstance (driving on an incline, for example) that causes the quantity of air to be insufficient for underhood cooling. This circumstance triggers the fan during constant-speed driving in order to assure additional airflow to that entering because of the movement of the car. The fan is triggered when a characteristic temperature in the underhood reaches some critical value and stops when the temperature is reduced, accounting for the oscillatory behavior in the evolution of the convective density. This convective density oscillatory behavior imposes oscillatory behavior on the surface and air temperatures, which impose oscillatory behavior on the radiative density and then on the overall density.

Figure 12 shows non-dimensional temperature and convective heat flux evolution at the cold box in TFP-2. In this figure temperature is non-dimensionalized by the stabilized temperature at the end of constant-speed driving phase, and convective heat flux with the heat flux at the beginning of each run. Let us consider the interval $\left[t_1;t_3\right]$. At t_1 the characteristic temperature of the underhood reaches its critical value and the fan is triggered. At the cold-box side, the air temperature is greater than the surface temperature. Then, with the fan triggered, the positive convective heat flux density and the air temperature increase between $\left[t_1;t_2\right]$. At t_2, the characteristic temperature is no longer critical and the fan stops. The interval $\left[t_2;t_3\right]$ corresponds to a decrease in fan velocity from the primary speed (2800 rpm) to zero (since the fan needs a short time to stop completely). Thus we observe in $\left[t_2;t_3\right]$ a decrease in the positive convective heat flux density (heat absorption by the cold box) as well as in the air temperature. This periodic variation of temperature has a frequency equal to 0.018 Hz. For example, in the triggered fan period $\left[t_1;t_2\right]$, the convective heat flux density increases from $0.16\varphi_0$ to $0.45\varphi_0$, causing the air temperature to increase from $0.96T_0$ to T_0. In addition, we observe also that the fan trigger penalizes the thermal situation at the cold-box side.

4- Conclusions

Car design in industrial automobile development projects is highly constrained by geometric restrictions induced by styling criteria and by the desire for ever higher-performance engines and better climate-control systems. Satisfying all the constraints requires placing a large number of components in underhood compartments. However, the underhood, already cramped, contains thermal systems (cooling, air conditioning, air charging, and the like) that are so large and complex that they cannot meet additional thermal performance requirements. These underhood aerothermal specifications give rise to airflows in the confined underhood space that entail complex aerothermal phenomena that involve the topology of internal flows, convective heat transfer in interaction with the internal flow topology, and radiative heat transfer in conjunction with the convective transfer.

In this study the convective and radiative heat fluxes exchanged between the heat sources and different components in an automobile underhood compartment are measured separately by a heat flux separation method. This heat flux database and its physical understanding constitute an essential part of underhood compartment aerothermal design and management. Some first steps in re-engineering of underhood aerothermal management can be the reorientation of air from sufficiently cooled zones to poorly cooled ones and the redistribution of the different air flow rates in the underhood region, the principal aim being always to minimize air inlet openings, and hence car energy consumption, by reducing aerodynamic cooling drag.

It was shown experimentally that the temperature and heat flux densities (overall, convective, and radiative) at the different components in the underhood compartment follow typically exponential tendencies in constant-speed driving, and in the thermal soak phases. It has also been shown that changes of slope in the evolutions of the temperature and heat flux densities are directly related to changes in the convection regime. In both the constant-speed driving and the thermal soak phases and for most of the tested components, it is the convective heat flux density that imposes its tendency on the overall heat flux density.

In addition to the above generic results, a large experimental database on temperature and heat flux densities has been constructed for different thermal functioning points at many components in the underhood compartment. These data can be used for validation of the CFD results for the car underhood compartment thermal predictions.

It should be emphasized that this study reveals that some of the cooling air flowing in the underhood compartment contributes to heating of some components rather than cooling them. Meanwhile, this cooling air increases also the vehicle aerodynamic drag. New architectures can be suggested by for example placing colder components upstream of hotter ones, or providing sub-compartments for components of close temperatures. Car underhood compartments designed based on these considerations will require less air for keeping the components at reasonable temperatures. This reduction in the cooling air will reduce the vehicle cooling drag and therefore, reduces car energy consumption. It also satisfies the styling requirements that insist on smaller front air openings for cars.

References

[1] E.P. Weidmann, J. Widemann, T. Binner, H. Reister, Underhood Temperature Analysis in Case of Natural Convection, SAE Paper 2005-01-2045, 2005

[2] E. Fournier, T. Bayne, Underhood Temperature Measurements of Four Vehicles, Motor Vehicle Fire Research Institute, Biokinetics and Associates, Ltd., Report R04-13, 2004

[3] E. Fournier, T. Bayne, Assessment of Thermocouple Attachment Methods for Measuring Vehicle Exhaust Temperature, Motor Vehicle Fire Research Institute, Biokinetics and Associates, Ltd., Report R06-23b for MVFRI, 2006

[4] E. Fournier, T. Bayne, Underhood Temperature Measurements, SAE Paper 2007-01-1393, 2007

[5] M.R. Jones, D.W. Fletcher, Thermal Performance Prediction of Front-End Heat-Exchange Modules, SAE Paper 2001-01-1765, 2001

[6] N. Francois, Using CFD for Heat Exchanger Development and Thermal Management, Valeo Engine Cooling, EACC, Frankfurt, Germany, June 29-30, 2005

[7] G. Xiao, Investigation of Conjugate Heat Transfer for Vehicle Underbody, SAE Paper 2008-01-1819

[8] O. Bailly, X. Baby, E. Fares, H. de Portzamparc, PIV and Numerical Correlations on the Laguna II Underhood Flow Field, Renault, SIA Congress, Lyon, France, October 26-27, 2005

[9] Z. Yang, J. Bozeman, F.Z. Shen, CFD for Flow Rate and Air Re-Circulation at Vehicle Idle Conditions, General Motors Corporation, SAE Paper 2004-01-0053, 2004

[10] A. Jerhamre, A. Jönson, Development and Validation of Coolant Temperature and Cooling Air Flow CFD Simulations at Volvo Cars, Volvo Car Corporation, SAE Paper 2004-01-0051, 2004

[11] E.P. Weidmann, H. Reister, T. Binner, Experimental and Numerical Investigations of Thermal Soak, SAE Paper 2008-01-0396, 2008

[12] T. Hormann, B. Lechner, W. Puntigam, T. Moshammer, R. Aimbauer, Numerical and Experimental Investigation of Flow and Temperature Fields Around Automotive Cooling Systems, SAE Paper 2005-01-2006, 2005

[13] RC01 Radiation / Convection (RADCON) Heat Flux Sensor, HUKSEFLUX™ THERMAL SENSORS brochure.

[14] M. Khaled, B. Garnier, F. Harambat, H. Peerhossaini, A New Method for Simultaneous Measurement of Convective and Radiative Heat Flux in Car Underhood Applications, Measurement Science and Technology Journal, (in press).

[15] M. Khaled, F. Harambat, Dispositif de Mesure de Flux Thermique et Méthode de Séparation des Flux Radiatif et Convectif, French patent application filed on February 10 2009, Patent n°0950799.

[16] M. Khaled, H. Peerhossaini, F. Harambat, Heat Transfer Mode Analysis in Complex Internal Flows, proceedings of ICHMT Congress, Hammamet, Tunisia, April 26 – May 1, 2009

Table and Figure captions

Table 1: Parameters defining the three tested thermal functioning points.

Figure 1: Schematic top view of the underhood instrumented positions.
Figure 2: Time evolution of overall heat flux densities measured by the two fluxmeters at the cold box side wall for TFP-3.
Figure 3: Time evolution of the overall, convective and radiative heat flux densities at the cold box side wall in TFP-3.
Figure 4: Time evolution of (a) temperature and (b) convective heat flux density at the cold box side region in TFP-3.
Figure 5: Time evolution at the cold box side wall for the three thermal functioning points of the: (a) overall heat flux density; (b) convective heat flux density; (c) radiative heat flux density.
Figure 6: Time evolution at air filter and charge air cooler outlet ducts in the constant-speed driving phase for TFP-1: (a) convective heat flux densities; (b) surface and air temperatures.
Figure 7: Experimental and theoretical evolution of temperature and convective heat flux density for TFP-1 in constant-speed driving phase for both cold box side wall and CAC inlet duct.
Figure 8: Time evolution of (a) temperature, (b) heat flux densities at the CAC outlet duct in thermal soak phase in TFP-1. The vertical lines correspond to the transition between the forced and natural convection parts of the thermal soak.
Figure 9: Dimensionless: (a) temperatures (b) overall heat flux density at all tested components for the three thermal functioning points.
Figure 10: Dimensionless convective heat transfer coefficients at different components for the three tested thermal functioning points.
Figure 11: Parameter evolution among the three thermal functioning points.
Figure 12: Surface temperature and convective heat flux oscillatory behaviors at the cold box side wall in TFP-2.

	V_W	V_{wind}	P	R	n
	$Km.h^{-1}$	$Km.h^{-1}$	KW	-	$tr.\min^{-1}$
TFP-1	90	90	69	5	2600
TFP-2	110	55	89	4	3800
TFP-3	130	130	98	5	3780

Table 1: Parameters defining the three tested thermal functioning points.

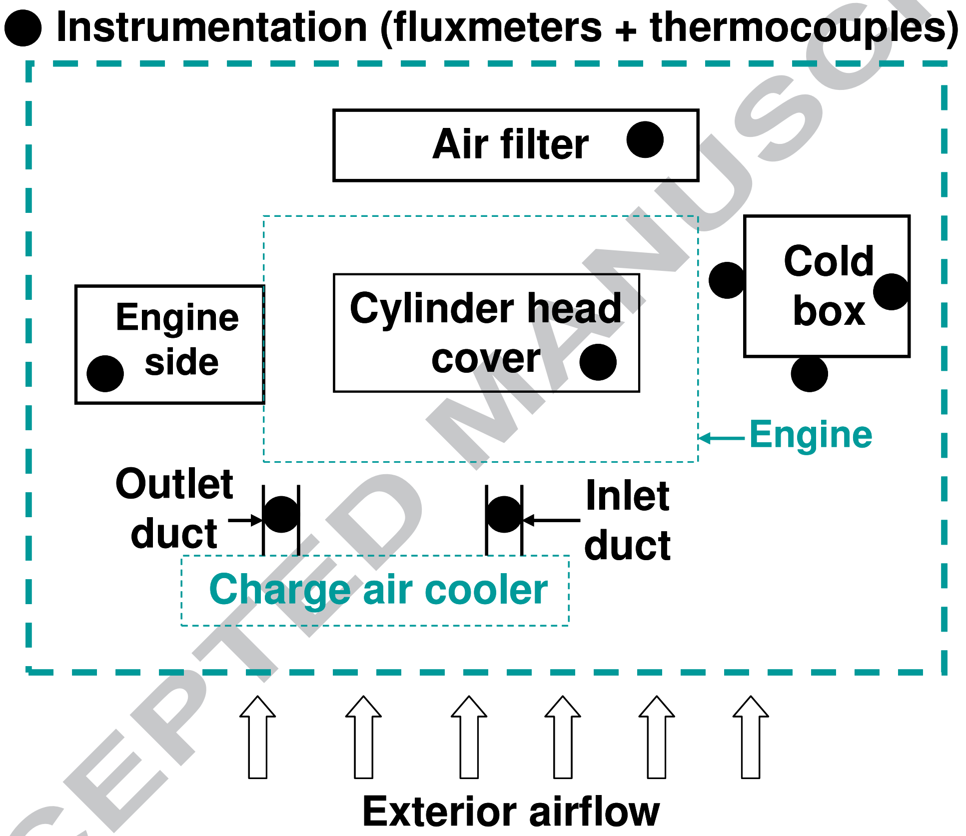

Figure 1: Schematic top view of the underhood instrumented positions.

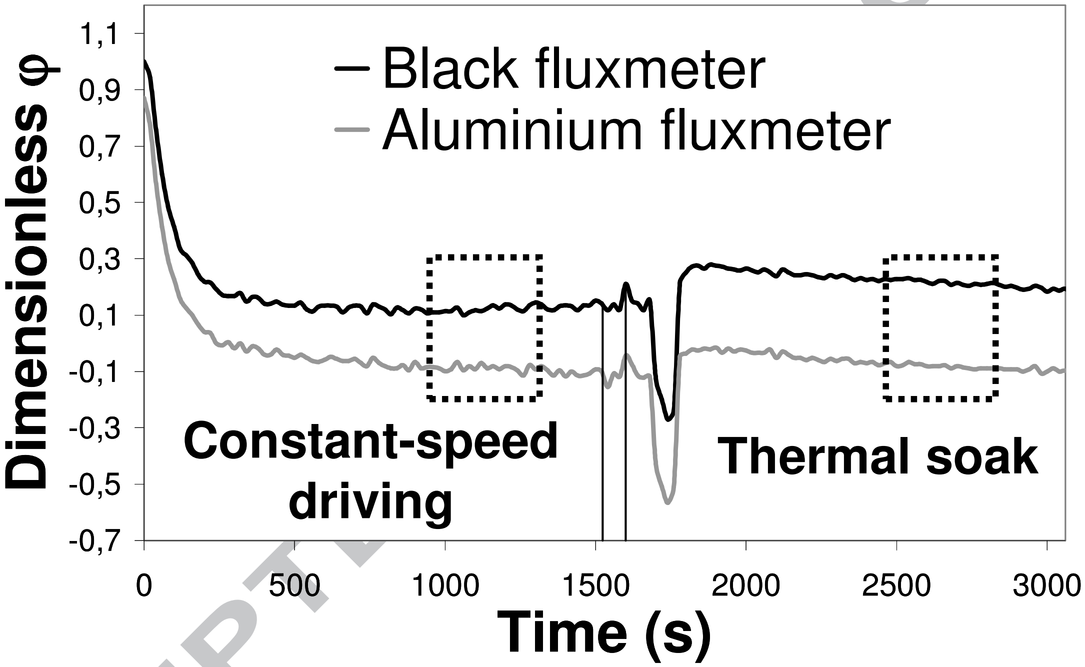

Figure 2: Time evolution of overall heat flux densities measured by the two fluxmeters at the cold box side wall for TFP-3.

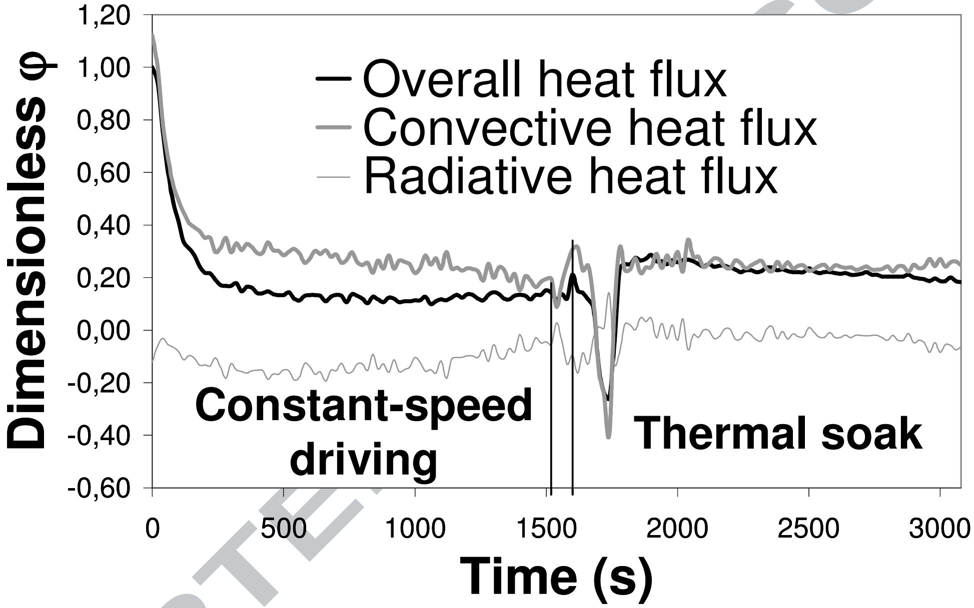

Figure 3: Time evolution of the overall, convective and radiative heat flux densities at the cold box side wall in TFP-3.

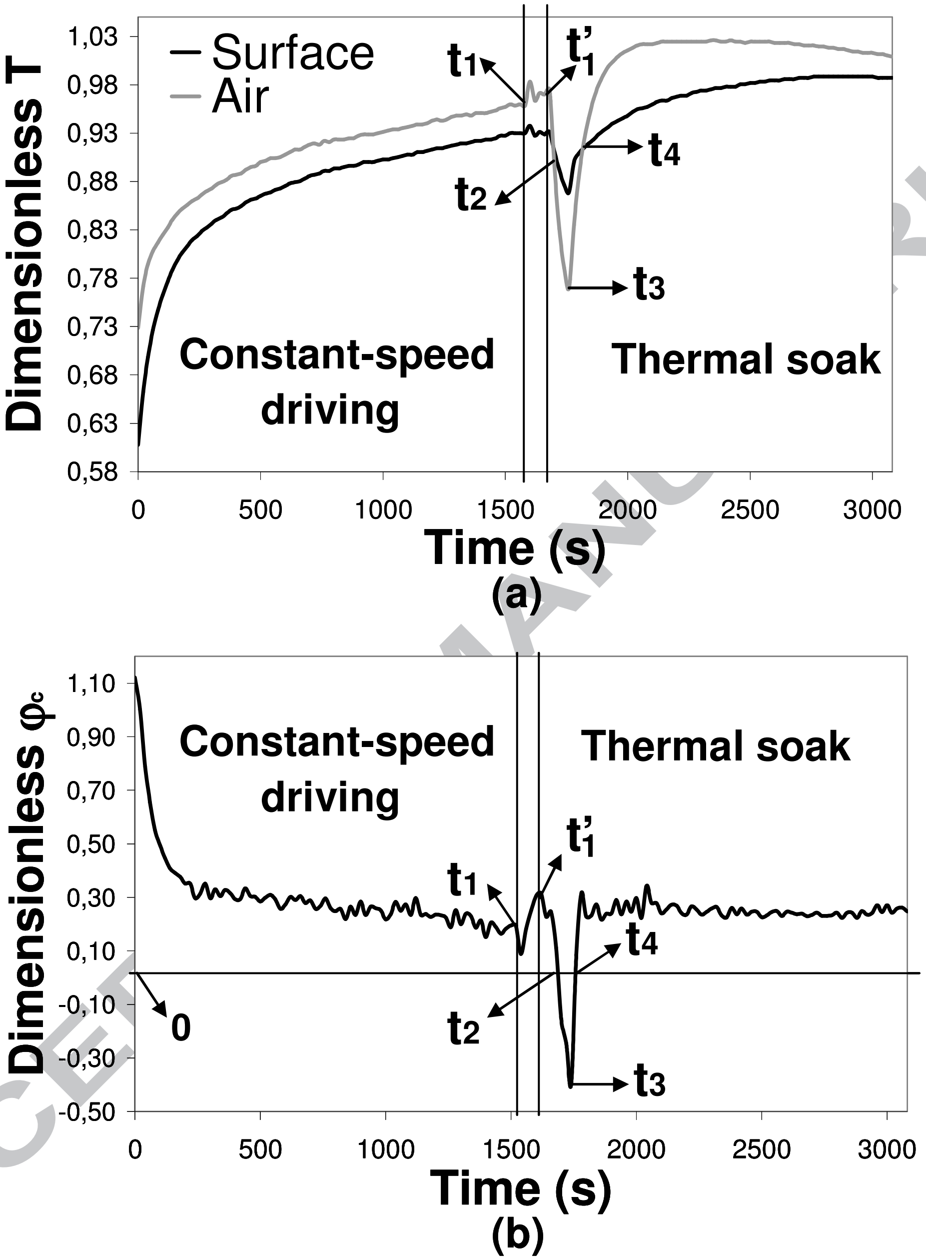

(a)

(b)

Figure 4: Time evolution of (a) temperature and (b) convective heat flux density at the cold box side region in TFP-3.

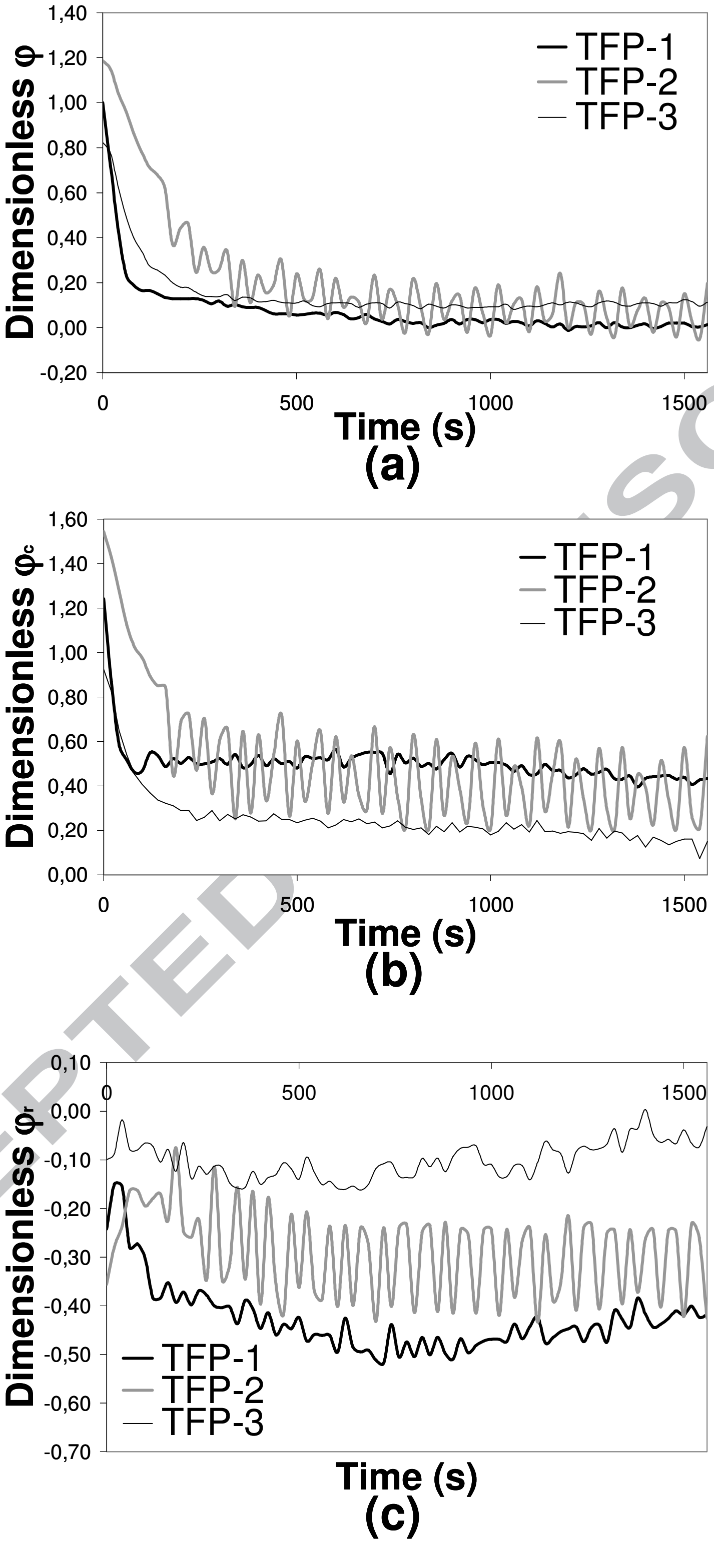

Figure 5: Time evolution at the cold box side wall for the three thermal functioning points of the: (a) overall heat flux density; (b) convective heat flux density; (c) radiative heat flux density.

.

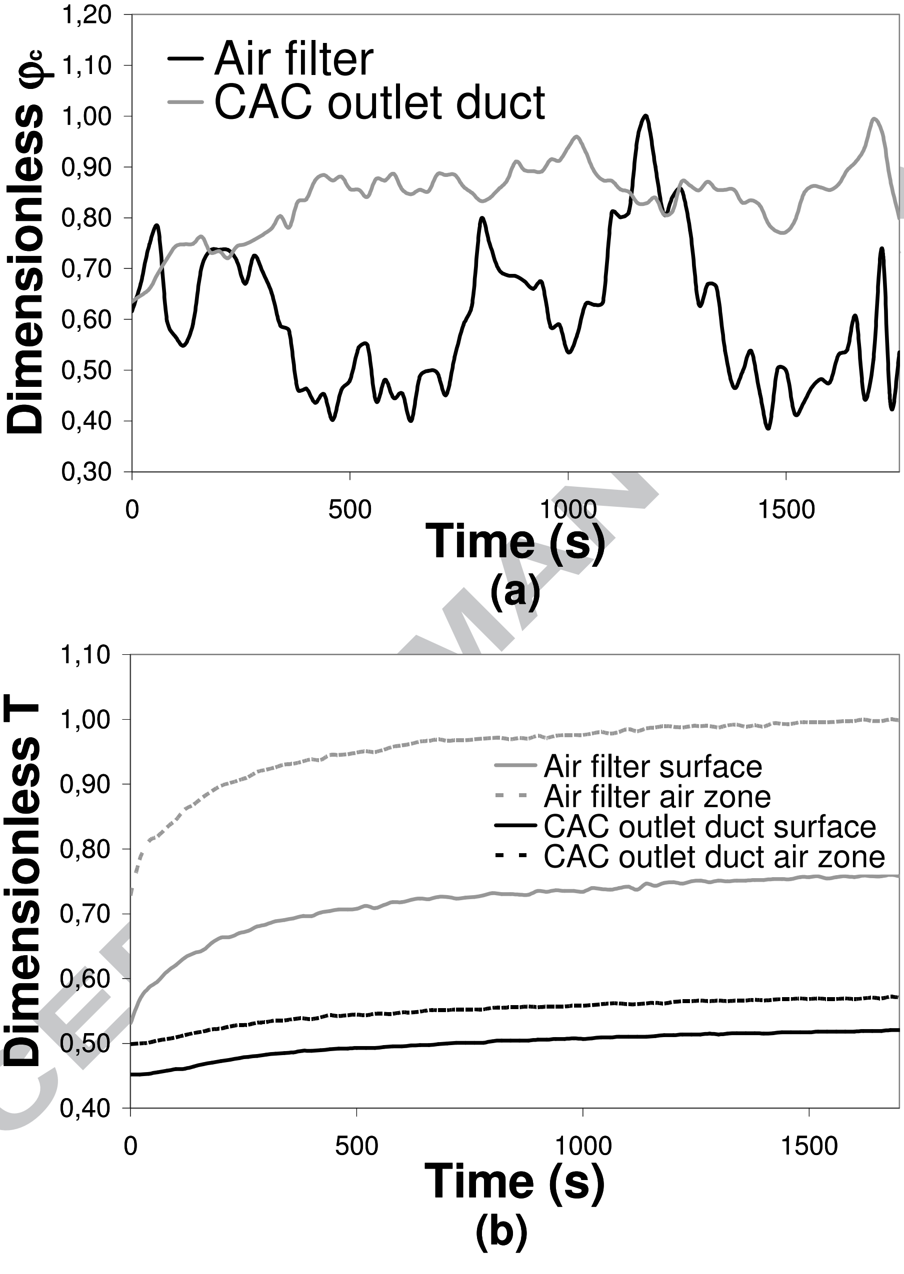

Figure 6: Time evolution at air filter and charge air cooler outlet ducts in the constant-speed driving phase for TFP-1: (a) convective heat flux densities; (b) surface and air temperatures.

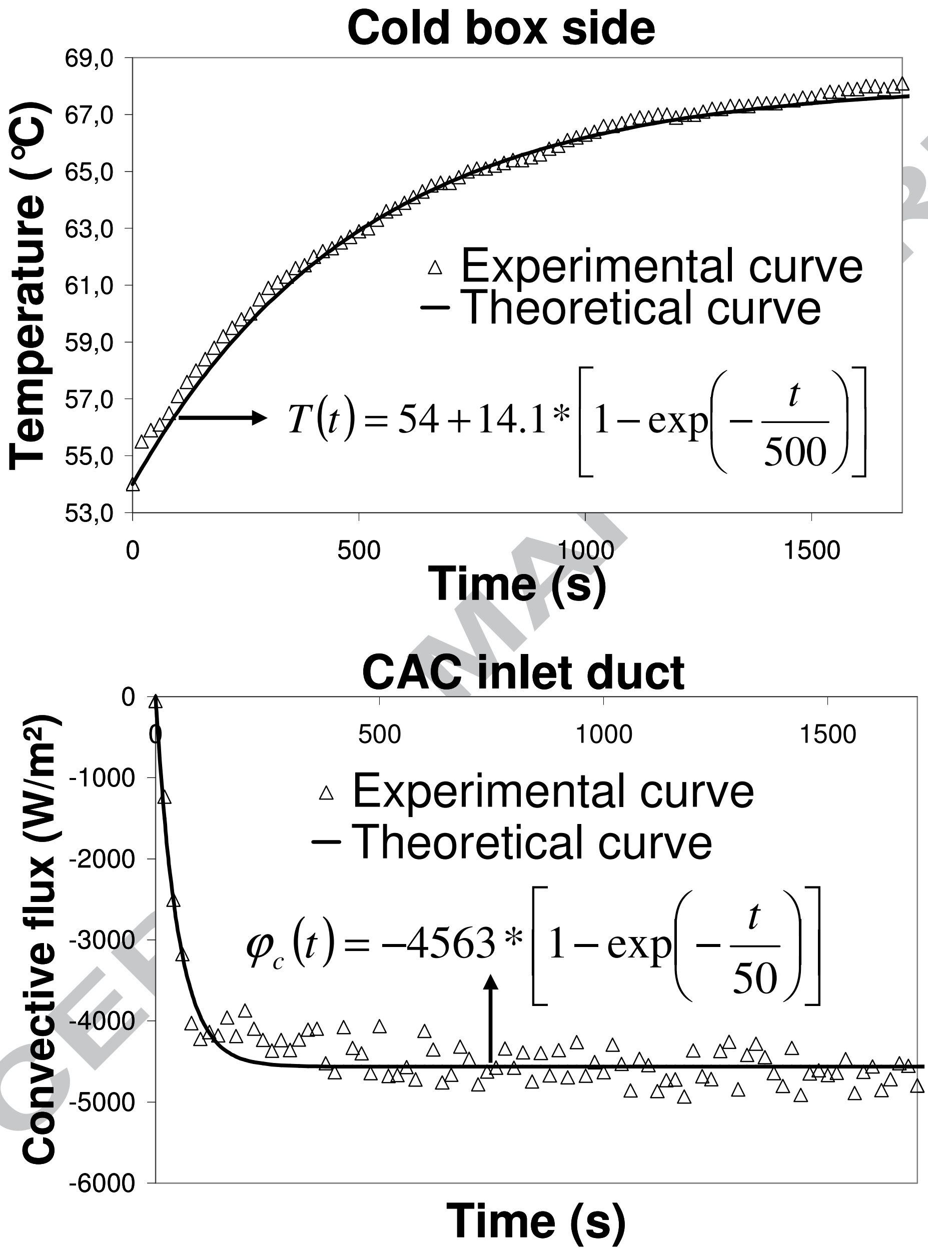

Figure 7: Experimental and theoretical evolution of temperature and convective heat flux density for TFP-1 in constant-speed driving phase for both cold box side wall and CAC inlet duct.

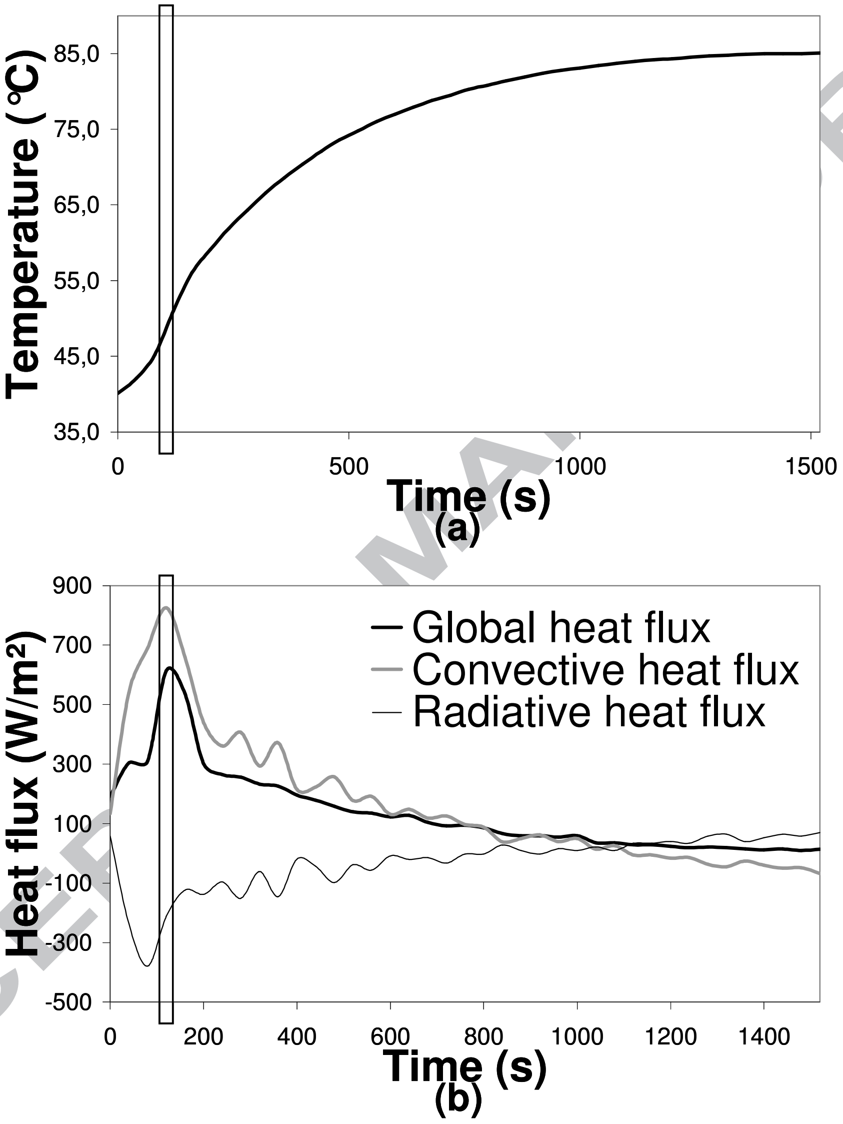

Figure 8: Time evolution of (a) temperature, (b) heat flux densities at the CAC outlet duct in thermal soak phase in TFP-1. The vertical lines correspond to the transition between the forced and natural convection parts of the thermal soak.

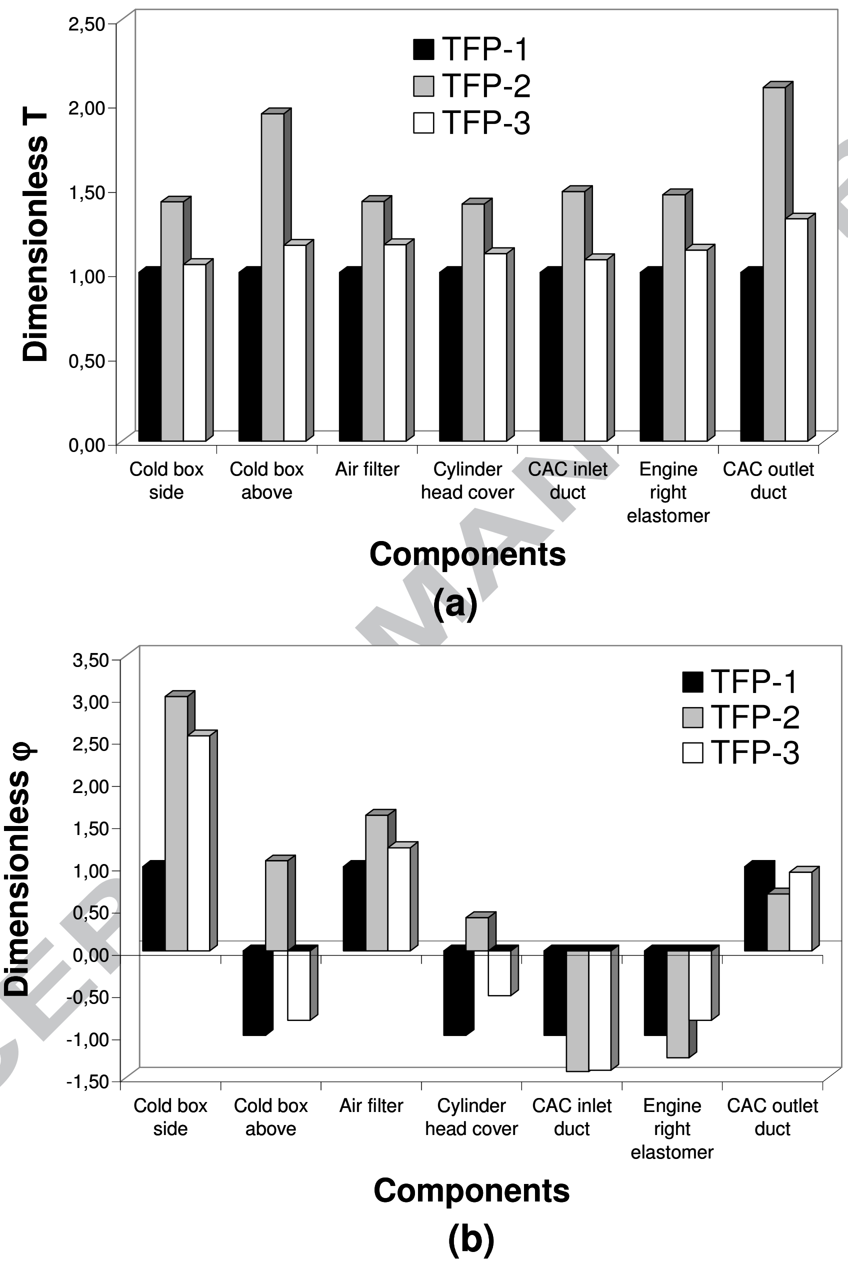

Figure 9: Dimensionless: (a) temperatures (b) overall heat flux density at all tested components for the three thermal functioning points.

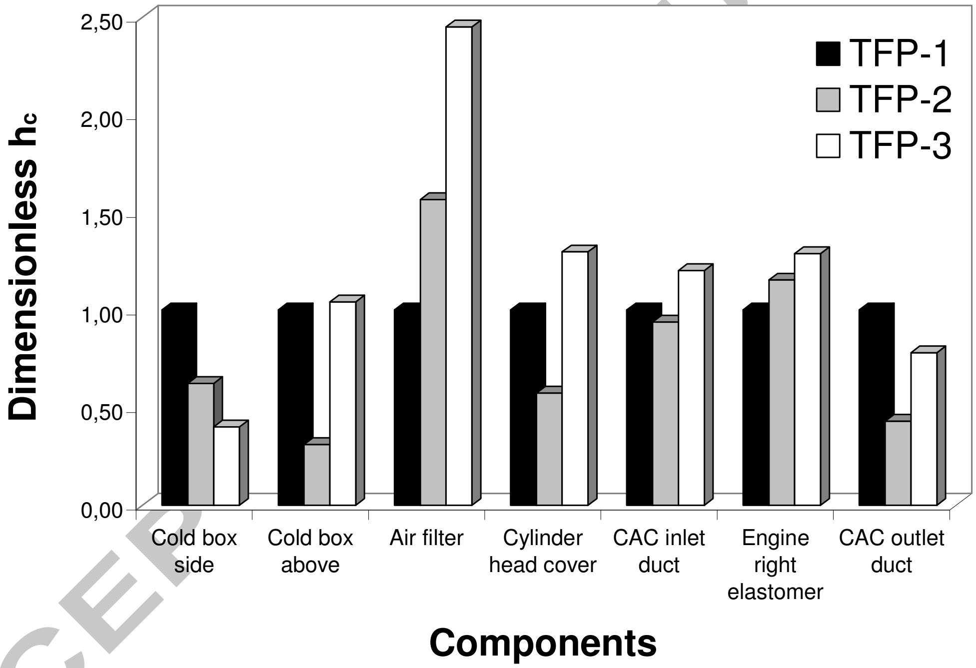

Figure 10: Dimensionless convective heat transfer coefficients at different components for the three tested thermal functioning points.

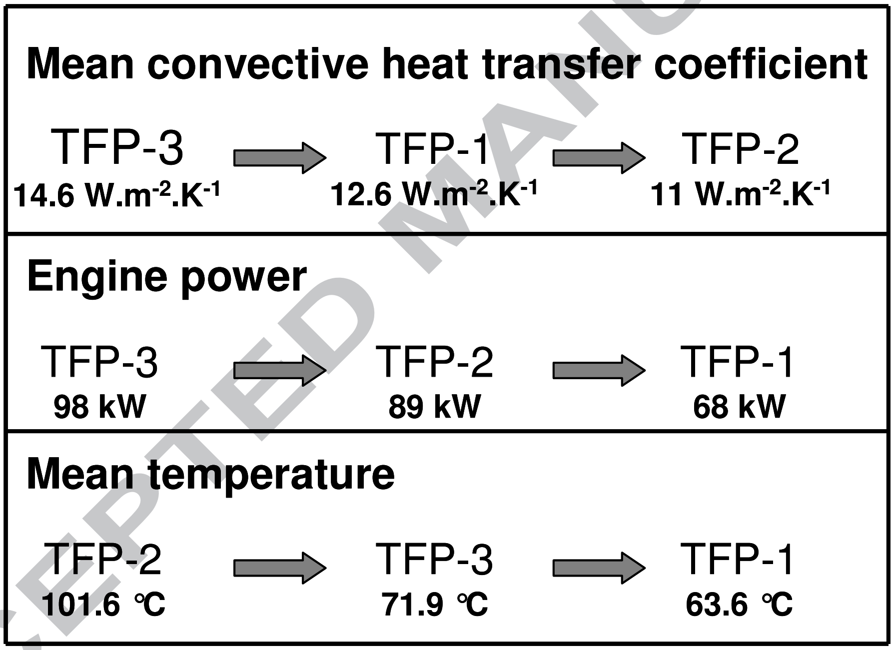

Figure 11: Parameter evolution among the three thermal functioning points.

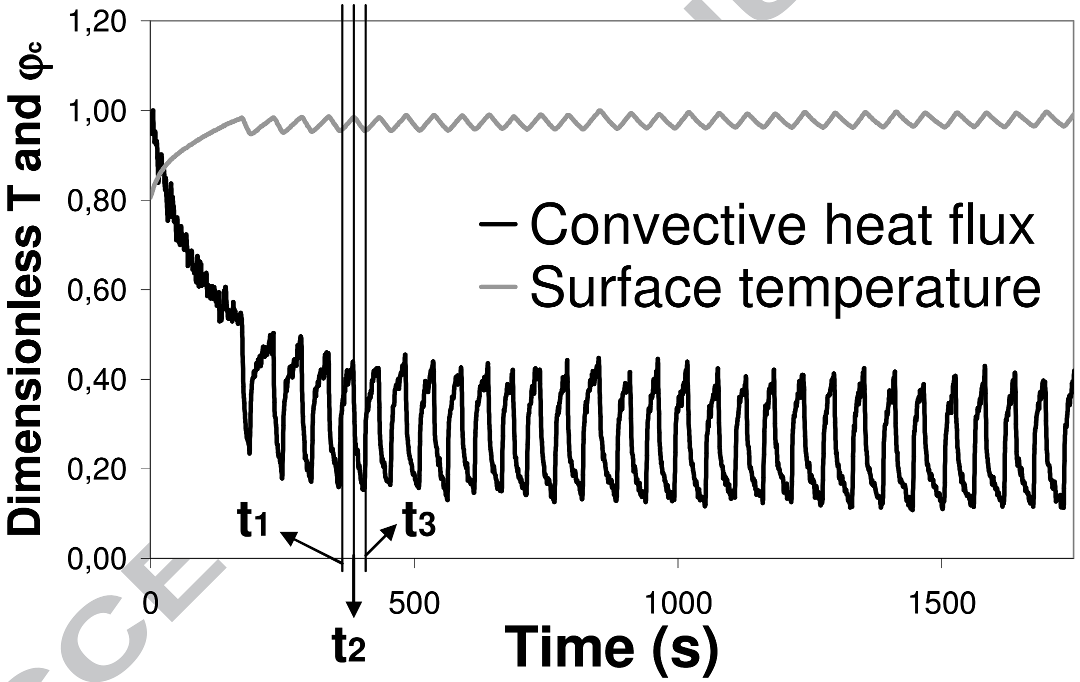

Figure 12: Surface temperature and convective heat flux oscillatory behaviors at the cold box side wall in TFP-2.